Climatology of Tropical Cyclone Rainfall Magnitude at Different Landfalling Stages: An Emphasis on After-Landfall Rain

OSCAR GUZMAN® AND HAIYAN JIANG®

^a Department of Earth and Environment, Florida International University, Miami, Florida

(Manuscript received 27 March 2022, in final form 22 May 2023, accepted 25 May 2023)

ABSTRACT: Estimating the magnitude of tropical cyclone (TC) rainfall at different landfalling stages is an important aspect of the TC forecast that directly affects the level of response from emergency managers. In this study, a climatology of the TC rainfall magnitude as a function of the location of the TC centers within distance intervals from the coast and the percentage of the raining area over the land is presented on a global scale. A total of 1834 TCs in the period from 2000 until 2019 are analyzed using satellite information to characterize the precipitation magnitude, volumetric rain, rainfall area, and axial-symmetric properties within the proposed landfalling categories, with an emphasis on the postlandfall stages. We found that TCs experience rainfall maxima in regions adjacent to the coast when more than 50% of their rainfall area is over the water. TC rainfall is also analyzed over the entire TC extent and the portion over land. When the total extent is considered, rainfall intensity, volumetric rain, and rainfall area increase with wind speed intensity. However, once it is quantified over the land only, we found that rainfall intensity exhibits a nearly perfect inversely proportional relation with the increase in TC rainfall area. In addition, when a TC with life maximum intensity of a major hurricane makes landfall as a tropical depression or tropical storm, it usually produces the largest spatial extent and the highest volumetric rain.

SIGNIFICANT STATEMENT: This study aims to describe the cycle of tropical cyclone (TC) precipitation magnitude through a new approach that defines the landfall categories as a function of the percentage of the TC precipitating area over the land and ocean, along with the location of the TC centers within distance intervals from the coast. Our central hypothesis is that TC rainfall should exhibit distinct features in the long-term satellite time series for each of the proposed stages. We particularly focused on the overland events due to their effects on human activities, finding that the TCs that at some point of their life cycle reached major hurricane strength and made landfall as a tropical storm or tropical depression produced the highest volumetric rain over the land surface. This research also presents key observational evidence of the relationship between the rain rate, raining area, and volumetric rain for landfalling TCs.

KEYWORDS: Rainfall; Tropical cyclones; Climatology; Microwave observations; Remote sensing

1. Introduction

When tropical cyclones (TCs) approach the coastline and make landfall, severe weather conditions can cause serious damage to coastal communities. The torrential precipitation produced by the storms poses one of the most dangerous threats to human life and infrastructure due to its potential to trigger inland freshwater flooding and mudslides (Willoughby 2012; Rappaport 2000). Therefore, a better understanding of the precipitation patterns at different landfalling stages is an extremely important input for emergency responders in catastrophes mitigation. A fundamental step in this effort is predicting specific areas within the TC structure that will develop the heaviest rainfall rates and their magnitude variations before, during, and after landfall events.

Several studies have examined the climatological features of tropical cyclone precipitation (TCP) and the factors that shape its intensity and geographic distribution over oceans and continents. For example, Jiang and Zipser (2010) calculated the contribution of TCP to the total precipitation balance over all the TC-prone basins, finding that TCs accounts for 4%–11% of the precipitation over the tropics but can

Corresponding author: Oscar Guzman, oguzm013@fiu.edu

account for as much as 50% in large regions over the open ocean. In a similar way, but focused on the continental part only, Prat and Nelson (2016) evaluated the TCP contribution over the land from 1998 to 2012, showing that an average of 3.5% of the total number of rainy days are caused by cyclonic activity. Their study also found that TCP-related days represent over 13% and 31% of extreme events but can account for more than 70% of extreme rainfall over higher-latitude areas. The study also reported that the major contribution usually occurs right after the peak of cyclonic activity in each global basin.

Some other specific basin-focused studies have reported the influence of TCP at local scales. For example, Bregy et al. (2020) characterized the total contribution over the eastern United States during the TC season, finding maxima on the Louisiana, North Carolina, and Texas coasts, decreasing farther inland at rates of approximately 6.2–6.7 mm km⁻¹; in their findings, they also report TCP is more closely linked to variations in the position of North Atlantic subtropical high than to the ENSO index. In the western North Pacific, especially for those TCs making landfall over China (including Taiwan and Hainan Islands), Ren et al. (2006) found that TCs significantly contribute to annual rainfall in the southern east coastal region, accounting for 20%–40% of the total annual balance. Similarly, and for the same basin, Zhang et al. (2017) revealed an increasing trend in the TCP based on the assessment of

extreme precipitation events that triggered floods over the Guangdong province. In such study, the authors also demonstrated that more than 60% of the largest hazardous floods in the northern and eastern parts of the province had been directly linked to TCP activity. In the Philippines, TC contribution to annual rainfall ranges from 6% in the southern regions to 54% over the northern regions (Bagtasa 2017). Over the South Pacific basin, continental Australia receives a contribution of between 30% and 70%, making it one of the regions of the globe where this fraction reaches the highest values (Dare et al. 2012). Finally, over the Indian ocean, Uddin et al. (2019) found that TCP contributes for about 8% of the total overland rainfall during 1998–2016 with a maximum occurrence during October–December (16%–18%) with more frequent occurrence in the Bay of Bengal.

In terms of the internal distribution of TCP, previous studies found that TCs over the ocean have a precipitation maximum in the front quadrants, either the left or the right forward half depending on the moving speed (Burpee and Black 1989; Rodgers et al. 1994). More recently, modeling results obtained by Kimball (2008) found that maximum rainfall occurring on the right side of the storm before landfall shifts to the left of the storm track during landfall (as the TC interacts with the coast); the author explains this variation in terms of the differential intrusion of dry air between the left and right sides of the storm using idealized landfalling modeling hurricanes. As TC makes landfall, interaction with land surface causes the wind and precipitation fields to decrease (Kaplan and DeMaria 1995), but the extent of the rainfall does not necessarily follow the same trend nor the same decreasing pace because of the complexity of the forcing factors that might drive rainfall distribution at landfall (Matyas 2010).

Internal TC rainfall distribution has also been analyzed under the influence of vertical wind shear (e.g., Corbosiero and Molinari 2002; Lonfat et al. 2004; Cecil 2007; Wingo and Cecil 2010). In most of these investigations, the rainfall variations are quantified as low wavenumber asymmetries using the Fourier decompositions over shear-relative rainfall distributions. The larger the asymmetry, the more variability in the internal spatial distribution may be explained (Yu et al. 2015). These studies coincide with the same conclusion: TCs over the ocean show downshear to downshear-left maximum in the wavenumber-1 asymmetry field. Besides, over land, Xu et al. (2014) and Yu et al. (2015, 2017) confirmed that this wind shear effect is still dominant even at different landfalling stages. Xu et al. (2014) also suggest that the magnitude of the rainfall asymmetry increases with the wind shear magnitude but decreases with the increasing TC rainfall intensity, and the wind shear effect is less efficient for TCs in environments of relatively low values of sea surface temperature (SST) and total precipitable water (TPW).

With reference to the TCP size, Kimball (2008) found that after landfall, the increasing friction results in broadened areas of accumulated precipitation with decreasing rain rates. This finding is consistent with observational studies analyzing TCP overland (Ren et al. 2006; Zhang et al. 2017; Bregy et al. 2020). In particular, Touma et al. (2019) refined previous investigations using the concept of life maximum intensity (LMI), stating that the highest median rainfall intensity and the largest median

spatial extent over land occur when major hurricanes have weakened to tropical storms, resulting in greater flood risk despite the weaker wind speeds. However, Touma's findings could potentially contradict previous investigations on the rainfall intensity assessment. For instance, using satellite precipitation retrievals, Jiang et al. (2008) found that the total volumetric rain after landfall is still highly dependent on the observed maximum wind speed and moisture parameters (e.g., the higher the TC max wind speed, the higher the rainfall intensity). So further research about the characteristics of the precipitation intensity and the volumetric rainfall for landfalling TCs is a must to clarify the reason for this potential contradiction.

Although the studies mentioned above characterize key features of TCP, there are few observational studies about its variation as a function of the location of the TC centers and the percentage of the raining area over the land on a global scale. In this paper, we explore the axial variations, distribution, and evolution of rainfall during the landfalling process of TC through a statistical approach that uses a homogeneous long-term time series of satellite retrievals. In addition, an emphasis on the postlandfall stage is presented by analyzing the TC LMI and the total volumetric rain, with the aim to investigate further the contradictions of previous studies about the behavior of the precipitation intensity on landfalling TCs, by taking advantage of the benefits of the spatial and temporal characteristics of the satellite data.

2. Data and methods

a. Data

The analysis period spans from June 2000 to December 2019, covering all the TC-prone global basins. A total of 1834 TCs are analyzed with a sample distribution of 315 in the North Atlantic basin (ATL), 363 in central and east Pacific (ECPA), 572 in western North Pacific (WNP), 114 in north Indian Ocean (NIO), 303 in the south Indian Ocean (SIO), and 167 in the South Pacific (SPA), respectively. Rainfall information is obtained from NASA Integrated Multi-satellitE Retrievals for the Global Precipitation Measurement (GPM) mission (IMERG) product version 6 (Huffman et al. 2019, 2020). IMERG combines multisatellite passive microwave (PMW) precipitation estimates, microwave-calibrated IR rain estimates, and rain gauge measurements into a homogeneous, high-quality retrieval. This study uses the final run version of IMERG with a spatial resolution of $0.1^{\circ} \times 0.1^{\circ}$ (nearly 10 km × 10 km) with a 3-hourly temporal resolution. Uncertainties about the IMERG products such as differences in the rainfall retrievals over the land and the ocean, availability of rain gauge station for calibration, and availability of enough microware measurements are not accounted in this study. We assumed the use of the IMERG final run as a reliable satellite product (as is) to study the TCP events at the best possible spatiotemporal scale on a global basis. Table 1 shows the number of IMERG files employed in this study grouped by TC intensities and basin; each file was converted to a GISreadable format and cataloged using a relational geodatabase for easier interaction with other geographics datasets.

TABLE 1. Number of best-track records with IMERG retrieved rainfall for TCs during 2000–19 in different TC intensity categories and different TC-prone basins.

Category/basin	ATL	ECPA	WNP	NIO	SIO	SPA	Total
Tropical depression	2694	4365	7135	1742	5614	2255	23 805
Tropical storm	6050	7169	9357	1862	6388	2791	33 617
Category 1	1624	1846	3613	331	1651	791	9856
Category 2	673	837	2033	104	822	399	4868
Category 3	611	768	1611	113	853	361	4317
Category 4	515	531	1796	103	581	276	3802
Category 5	126	53	542	21	68	66	876
Total	12 293	15 569	26 087	4276	15 977	6939	81 141

TC attributes such as center coordinates, time, and maximum wind speed are obtained from the International Best Track Archive for Climate Stewardship (IBTrACS version 4; Knapp et al. 2018) in both point and line vector topologies. To maximize the temporal match with the IMERG overpasses, we used the 3-hourly positions obtained by spline interpolation from the original 6-hourly best-track coordinates, as reported in columns 9 and 10 in IBTrACS. Several filters were applied to the best-track database to maximize the quality of the data, including the removal of subtropical and extratropical positions; the omission of records with low-quality attributes in columns 8, 14, 17, 23, and 26 of the IBTrACS; and the removal of poleward positions beyond a latitude of 35° to minimize the effect posttropical storms in the results. Both developing and nondeveloping tropical depressions were included in the final geographic database. Considering IBTrACS is a collection of other best-track datasets created by different WMO agencies, discrepancies in the reported values were resolved by performing a meticulous verification at the geographic borders between reporting agencies (e.g., between the U.S. agencies and JMA near 180° longitude) In all cases, the values reported from U.S. agencies were in the first order of eligibility (NOAA NHC and JTWC). No adjustment was made for differences in wind speed averaging periods between the reported values of each WMO agency.

Environmental conditions around the storms are obtained from the Statistical Hurricane Intensity Prediction Scheme

(SHIPS; last updated: April 2020) developmental dataset, which includes 6-h retrievals of observational and derived data over various annular regions calculated from the TC center (DeMaria and Kaplan 1994, 1999; DeMaria et al. 2005; Schumacher et al. 2013). In this study, we selected four SHIPS environmental parameters to be examined at each landfall stage: Reynolds sea surface temperature (RSST), wind shear with vortex removed and averaged from 0 to 500 km (SHDC), wind shear heading averaged from 0 to 500 km (SHDD), and total precipitable water between 0 and 500 km. Only the values at the initial time (t = 0) are employed in our analyses.

b. Definition of stages relative to landfall

Previous studies of rainfall distributions in landfalling TCs classified stages relative to landfall in different ways. Jiang et al. (2008) grouped Tropical Rainfall Measuring Mission (TRMM) 3B42 overpasses into ocean, mixed, and land groups using the percent coverage of raining area over land or ocean. For each 3B42 snapshot within a 5° radius of the TC center, if greater than 60% of the raining area was over the ocean (land), this overpass was attributed to ocean (land) group. If 40%–60% of the raining area is over land/ocean, this overpass was grouped as mixed. Xu et al. (2014) defined three landfalling stages of TRMM 3B42 overpasses based on the TC center's proximity to the coast. If the TC center was 400 to 700 km, 0 to 300/400 km, and -200 to 0 km from the coast, this overpass

TABLE 2. Classifications of various stages before, during, and after TC landfall in Jiang et al. (2008), Xu et al. (2014), Yu et al. (2017), and this study.

	Jiang et al. (2008)	Xu et al. (2014)	Yu et al. (2017)	This study		
Before landfall	Ocean: TC raining area > 60% over ocean	Offshore: TC center 400–700 km away from coast	Stage I: 24 h prior to landfall	Open Ocean	Ocean: TC center >700 km away from coast Offshore: TC center 400– 700 km away from coast	
During landfall	Mixed: TC raining area 40%–60% over land	Preland: TC center 0-300/400 km away from coast	Stage II: at the time of landfall	Adjacent to the coast: TC center 0-400 km away from the coast	Near-Land I: TC raining area < 50% over land Near-Land II: TC raining area ≥ 50% over land	
After landfall	Land: TC raining area > 60% over land	After-land: TC center -200-0 km away from coast	Stage III: 24 h after landfall	Overland: TC center is over land	Overland I: TC raining area < 50% over land Overland II: TC raining area ≥ 50% and < 100% over land Overland III: TC raining area 100% over land	

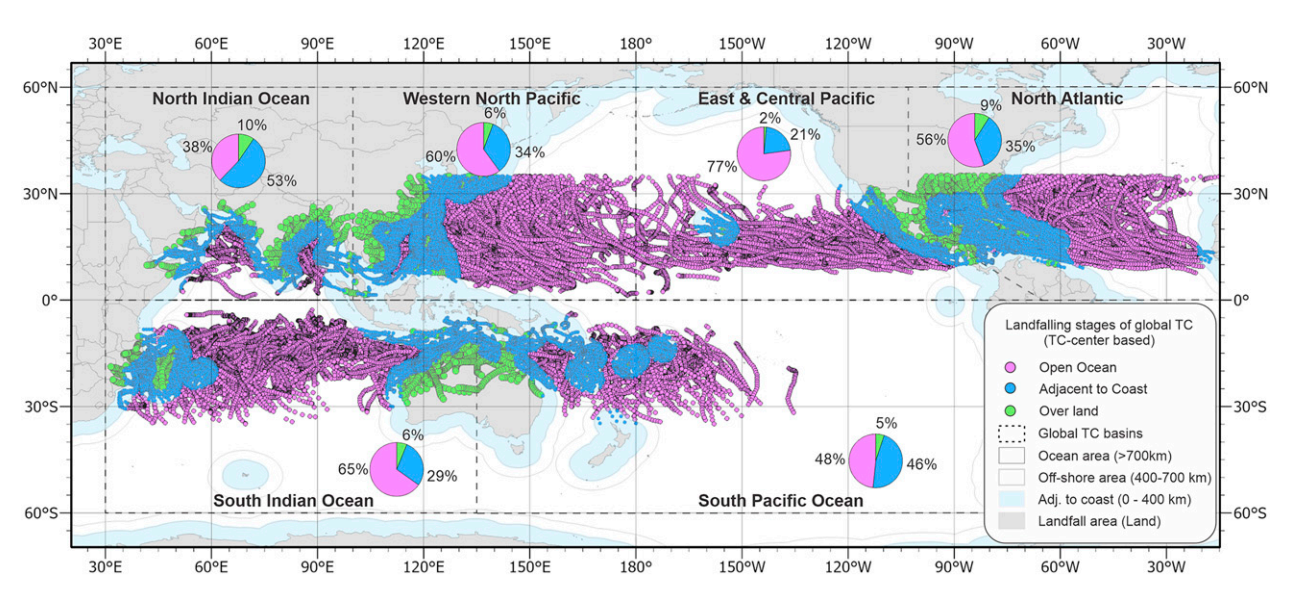


FIG. 1. Locations of TC centers for all best-track records as a function of the three main landfalling stages. Magenta color represents TC centers over the open ocean, blue color represents TC centers adjacent to the coast, and green color represents TC centers over land. Pie charts show the percent contribution of each landfall stage per global basin. Regions corresponding to each category as the distance from the shoreline are also shown. Land surfaces with areas less than 1400 km² are not considered.

was defined as offshore, preland, and aft-land, respectively. Yu et al. (2017) described three stages associated with before, during, and after landfall based on the observation time of 3B42 relative to the TC center's landfall time, with stage I, II, and III defined as 24 h prior to, at the time of, and after the TC center's landfall. Table 2 summarizes the classifications in these three studies

Note that the classifications in the last two studies only considered the TC center's landfall, while the first study only considered the raining area's landfall. A good classification method should consider both. Yu et al.'s (2017) definition is based on the period before or after the TC center's landfall, which depends not only on how far the observation is close to the coast or inland but also on the storm translation speed. Therefore, in this research, we adopted both Jiang et al.'s (2008) and Xu et al.'s (2014) approaches. As shown in Table 2, we classified into three main categories, including Open Ocean, Adjacent to the Coast, and Overland. In a vast majority of cases, these categories follow a perfect chronological order (before, during, and after landfall). However, careful exceptions must be considered when analyzing TC experiencing multiple landfalls or moving backward across the proposed landfalling categories. The Open Ocean category is further divided into two subcategories: Ocean is for TCs with centers greater than 700 km away from the coast, and Offshore is for TCs with their centers 400 to 700 km away from the coast. The Adjacent to the Coast category is defined as TCs with their centers 0 to 400 km away from the coast. This category is further divided into two subcategories: Near-Land I and Near-Land II, based on how many percentages of the TC raining area are over land. The Overland category is defined as TCs with their centers over land. This category is further divided into three subcategories: Overland I, Overland II, and Overland III, based on how many

percentages of the TC raining area are over land. Notice that we do not explicitly consider time criteria in proposed landfalling categories (e.g., hours before or after the landfall event). Therefore, for comparison purposes with previous studies, our nearly equivalent definitions of before, during, and after landfall are based merely on spatial criteria with a sense of a temporal evolution implicit, but not on a pure and perfect temporal scale, like that suggested by Yu et al. (2017).

With these definitions, a geospatial classification of the best-track record was performed to obtain the TC samples for each landfall stage. As a first step, each TC center is assigned to a geographic region representing Open Ocean, Adjacent to the Coast, and Overland, as shown in Fig. 1. Several minimum island sizes were tested during the buffer operation to obtain consistent areas for each category across all the TC-prone global basins. This procedure was particularly sensitive for the North Atlantic and South Pacific basins due to the presence of large chains of islands. A final threshold of 1400 km² was employed to remove minor islands. Figure 1 shows a map with the classification of best-track records and the percentual distribution of each basin. It can be noticed that globally the majority of the TC positions fall into the Open Ocean category (48%-77%), followed by Adjacent to the Coast (21%-53%), and ending with Overland records (2%–10%). In addition, each basin exhibits unique features. For instance, ECPA is less prone to landfalling events; in contrast, ATL, WNP, and NIO exhibit the highest susceptibility. Table 3 shows the same best-track records as Fig. 1 but normalizing by storm ID (including named and no-named TC). Under the above considerations, global TCs have a fraction of landfall near 38%. As the second step, each Tropical Cyclone Precipitation Feature (TCPF; see the details below in section 2c) is determined. Its areal portion over both land and ocean is calculated to

TABLE 3. Number of TCs and landfalling TCs (in parentheses) categorized by season and basin during the period 2000–19. Note that the fraction of landfall TCs is calculated as TC center over land. Only land surfaces greater than 1400 km² are considered. Values for Southern Hemisphere basins during 2000 are not available.

Season/basin	ATL	ECPA	WNP	NIO	SIO	SPA	Total
2000	18 (5)	19 (2)	31 (12)	4 (3)	N/A	N/A	72 (22)
2001	16 (7)	17 (1)	33 (17)	5 (2)	16 (5)	8 (2)	95 (34)
2002	14 (8)	16 (2)	31 (12)	5 (3)	17 (5)	9 (4)	92 (34)
2003	21 (8)	16 (5)	27 (14)	4 (3)	19 (7)	11 (2)	98 (39)
2004	15 (7)	16 (2)	32 (14)	6 (2)	18 (8)	7 (3)	94 (36)
2005	29 (15)	16 ()	25 (15)	7 (3)	19 (3)	8 (2)	104 (38)
2006	9 (2)	21 (2)	26 (16)	7 (5)	16 (5)	8 (2)	87 (32)
2007	14 (9)	15 (2)	27 (12)	6 (5)	14 (7)	10(1)	86 (36)
2008	16 (10)	18 (4)	27 (13)	7 (7)	20 (6)	9 (2)	97 (42)
2009	9 (2)	20 (3)	28 (13)	5 (4)	18 (5)	10(2)	90 (29)
2010	21 (8)	12 (3)	19 (11)	5 (4)	15 (5)	10 (4)	82 (35)
2011	18 (5)	13 (3)	27 (12)	6 (3)	13 (6)	9 (3)	86 (32)
2012	18 (6)	17 (1)	27 (12)	4 (3)	17 (6)	4(0)	87 (28)
2013	14 (5)	18 (4)	33 (18)	7 (7)	16 (3)	8 (1)	96 (38)
2014	9 (2)	21 (2)	23 (13)	5 (2)	15 (5)	11 (6)	84 (30)
2015	11 (3)	22 (4)	28 (13)	4(2)	18 (6)	9 (2)	92 (30)
2016	16 (9)	21 (3)	30 (14)	5 (2)	9 (1)	11 (3)	92 (32)
2017	18 (10)	20 (5)	33 (23)	5 (3)	11 (4)	8 (3)	95 (48)
2018	14 (4)	25 (5)	35 (21)	9 (9)	13 (6)	8 (2)	104 (47)
2019	15 (4)	20 (3)	30 (15)	8 (4)	19 (4)	9 (4)	101 (34)
Total	315 (129)	363 (56)	572 (290)	114 (76)	303 (97)	167 (48)	1834 (696)
TC landfall fraction	41%	15%	51%	67%	32%	29%	38%

refine at the subcategory level within each landfall stage. Table 4 summarizes the final sample size obtained for each category across global basins.

c. Precipitation features and axisymmetric decompositions

As a prerequisite to calculating TC rain-associated parameters, a definition of the TC rainfall area must be adopted. Therefore, we define the TC raining area using the concept of TCPF suggested by Jiang and Zipser (2010). Under the TCPF framework, a precipitation cell (precipitation feature) is delineated by contiguous grouping pixels that comply with a selection criterion. In this study, only IMERG pixels with a rain rate greater than 0.1 mm h⁻¹ are chosen to be part of each precipitation cell, zero values and nondata values are excluded from the calculations. Furthermore, to be qualified as TCPF, the distance between the TC center and the geometric center of each valid cell must be less than 500 km. A geodatabase

with raster and vector versions of the TCPF at each IMERG observation time was created to subsequently allow the match with the best-track and SHIPS databases through predesigned foreign keys within a relational database model.

The axisymmetric decomposition is performed by determining the azimuthal mean rainfall rate in 100 steps of 10-km wide annuli from the storm center outward to the 1000 km. Only pixels belonging to TCPF are considered in calculating the averages to avoid contamination from neighboring non-TC precipitation features. Since 10-km is about the IMERG spatial resolution, the algorithm only includes pixels when more than half of its size is within the annulus. Finally, the 2D composites of rainfall rate distribution rotated relative vertical wind shear (the SHDD parameter from SHIPS) are calculated for different TC landfall stages as a function of the storm translation speed and environmental variables. The shear directions of Southern Hemisphere overpasses are flipped around the motion direction to be consistent with the

TABLE 4. Number of selected satellite overpasses of IMERG records over TC centers in different landfall stages.

Landfall stage	Subcategory	ATL	ECPA	WNP	NIO	SIO	SPA	Total
Open Ocean (TC center over open ocean)	Ocean (>700 km)	5659	8814	121 30	287	8237	1519	36 646
	Offshore (400–700 km)	1189	3196	3544	1329	2184	1841	13 283
Adjacent to the Coast (0-400 km)	Near-Land I < 50% over land	4129	3229	8608	2125	4460	3060	25 611
	Near-Land II $\geq 50\%$ over land	204	89	309	126	99	165	992
Overland (center over land)	Overland I $< 50\%$ over land	356	174	666	86	332	109	1723
	Overland II $\geq 50\%$ and $< 95\%$ over land	661	67	780	302	574	216	2600
	Overland III > 95% over land	95	0	50	21	91	29	286
Total		12 293	15 569	26087	4276	15 977	6939	81 141

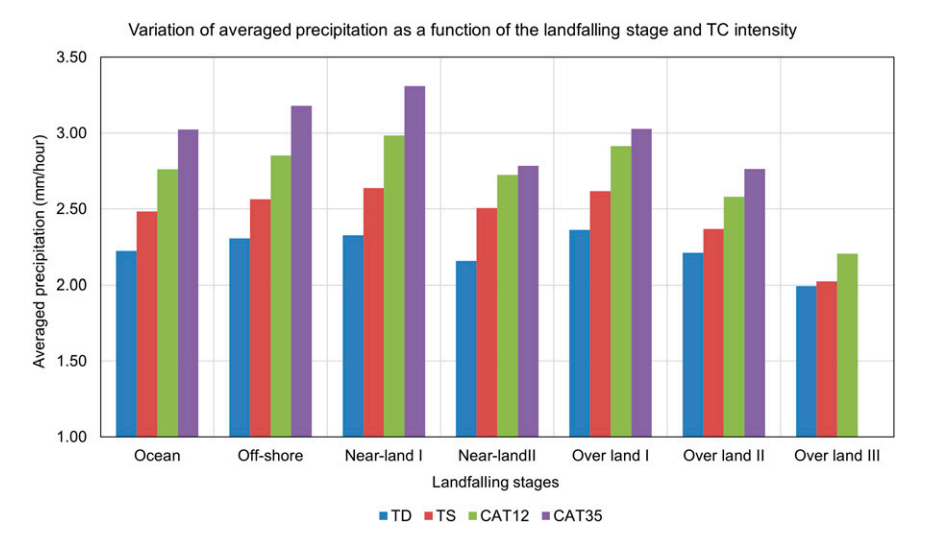


FIG. 2. Variation of the mean tropical cyclone precipitation intensity (rain rate) as a function of the landfall stage for different storm intensities.

Northern Hemisphere frame of reference and to account for the Coriolis effect, as explained in Chen et al. (2006). We stratified the motion speed into two categories as suggested by Pei and Jiang (2018): Low motions speed ($0 < 5 \text{ m s}^{-1}$) and fast motion speed ($\geq 5 \text{ m s}^{-1}$). In the case of the wind shear magnitude, it was stratified into two categories looking for a 50%–50% split: low shear (0–8 m s⁻¹) and high shear (>8 m s⁻¹). TPW was also divided into two categories looking for a 50%–50% split: low TPW (0–60 mm) and high TPW (>60 mm), and finally, the sea surface temperature was also stratified into two categories (by following Cecil 2007): Low SST ($\leq 28^{\circ}$ C) and high SST ($\geq 28^{\circ}$ C). Results of this classification for the Open Ocean, Adjacent to the Coast, and Overland landfall stages are presented in the discussion section.

d. Area and volumetric rain analysis over landfalling TCs

For those TCs with tracks that at some point during their lifetime fall in the postlandfall categories (i.e., Overland I, Overland II, and Overland III), we identified the individual LMI by looking at the maximum sustained wind speed and categorizing this value into an abbreviated intensity scale that consists of four categories: tropical depression (TD), tropical storms (TS), minor hurricanes (CAT12), and major hurricanes (CAT35). In this way, each TC track snapshot can be categorized by combining its point intensity (current) and the LMI. For instance, TD/CAT35 indicates that the storm intensity at the current satellite observation position is a TD and that storm at some moment during its lifetime reached CAT35. Thus, there are 10 possible point-intensity–LMI combinations TD/TD, TD/TS, TD/CAT12, TD/CAT35, TS/TS, TS/CAT12, TS/CAT35, CAT12/CAT12, CAT12/CAT35, and CAT35/CAT35.

As a second step, the average rainfall rates and the precipitation area for each satellite overpass are calculated. This pro-

cedure is applied over the raining pixels obtained from the TCPF method suggested by Jiang and Zipser (2010), that is, precipitation cells with values greater than 0.1 mm h⁻¹ in the IMERG file. Then, average rainfall rate values per overpass are categorized following the proposed landfalling stages, the storm intensity in the Saffir-Simpson scale, and the point-intensity-LMI schemes. For each category, an averaged value is obtained and analyzed (average per category of the averaged raining pixels per overpass).

The last step calculates the volumetric rain over the total TC area and over the effective land portion (rain pixels over land only). Although both averages are reported, this procedure was performed to facilitate an objective comparison with studies working with rainfall over land and provide a more realistic estimation of the rainfall magnitude that affects human activities inland. In calculating rain over land, a raster map of $0.1^{\circ} \times 0.1^{\circ}$ containing the continental and island polygons was employed to distinguish between land and ocean pixels by looking for a perfect match with the spatial resolution of the satellite IMERG rain data. The total volumetric rain of each overpass is calculated by multiplying the average TC rain by the TC area.

3. Results and discussion

a. TC precipitation over the open ocean

During the TC travel over the open ocean, TCP experiences a homogeneous growth mainly controlled by TC wind intensity and environmental conditions (Jiang et al. 2008). As shown in Fig. 2, for the two open ocean categories (Ocean and Offshore), it can be noticed that the averaged TCP is >higher for storms closer to the land, this behavior is consistent with the traditional strengthening trend of TC characteristics when TCs move freely over the ocean with

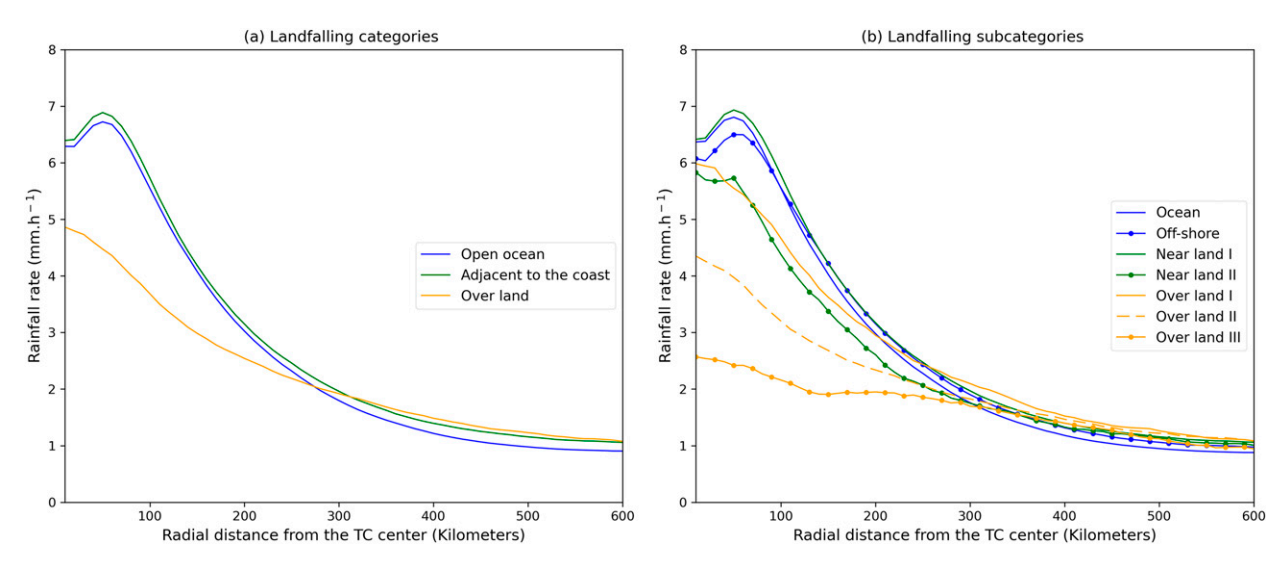


FIG. 3. Radial distribution on azimuthally averaged rainfall rate categorized by landfalling stages: (a) Division as the distance from the land for Open Ocean, Adjacent to the Coast, and Overland. (b) Subdivision of landfalling stages combining distance from the land and percentage of the raining area over land/ocean.

full access to surface fluxes of latent heat that favor its intensification. From the axisymmetric standpoint, Fig. 3 shows that globally, TC radial distribution is well-defined and nearly follows the classic wind patterns reported in the TC literature (e.g., Holland 1980; Holland et al. 2010). For the interbasin

differences, Fig. 4 shows the axisymmetric patterns for each global basin. In general, the TCP intensity is slightly higher as the TC falls in a landfall category closer to the land, except in the WNP and ECPA basins, where Ocean profiles are higher than Offshore, particularly at the inner core level.

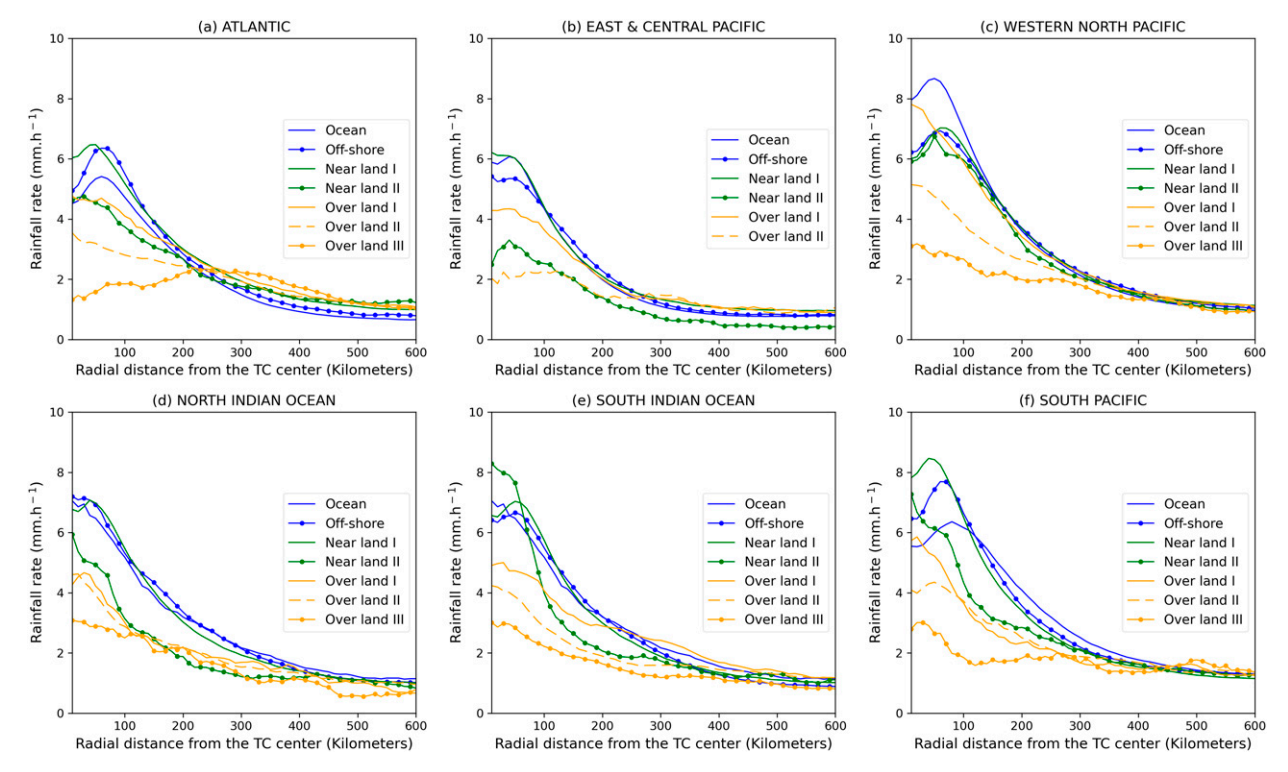


FIG. 4. Radial distribution of azimuthally averaged rainfall rate for different landfall stages in (a) ATL, (b) ECPA, (c)WNP, (d). NIO, (e) SIO, and (f) SPA basins.

b. TC precipitation adjacent to the coast

In the case of the two Adjacent to the Coast categories, we found opposite behavior (Fig. 2). For the first part, when at least half of the TCP area remains over the ocean (Near-Land I), the average precipitation reaches its maximum across all the landfalling categories. In contrast, once the TCP area exceeds 50% over land (Near-Land II), there is lower precipitation production caused by the abrupt change in the surface predominance from water to land. Across the Adjacent to the Coast stages, the azimuthally averaged profiles of Fig. 3 still show an axisymmetric structure. However, in the Near-Land II stage, eye patterns in TCs begin to disappear at the inner-core level (Fig. 3).

For the interbasin differences, each basin exhibits a different level of separation between the axisymmetric profiles of both Adjacent to the Coast stages (Fig. 4), perhaps because of specific geographic conditions. However, a formal explanation of such differences (and others between basins) is difficult to determine and beyond the scope of the present research.

c. TC precipitation over the land

Overland stages show their highest TCP values in storms with up to 50% of their TCP area over the ocean, followed by lower values in the categories where the TCP area moves inland. Interestingly, the Overland I region reveals higher rainfall rates than Near-Land II. However, a rigorous chronological order between the two categories is difficult to establish under the proposed landfalling categories. In addition, data with better temporal resolution would be required for a more detailed analysis of this potential precipitation enhancement during the first part of the stages over the land.

TCs in the Near-Land II and Overland I categories exhibit similar axisymmetric properties in most of the panels in Figs. 3 and 4 with minor variations. We noticed that these profiles are difficult to differentiate due to the oscillation in the average precipitation rates near the landfall time. Although our proposed classification of landfalling stages is intended to follow an evolution order in terms of the TCP cycle, the irregular shape of TCP areas near the coastline can lead to two imperfections: 1) storms with TC centers overland containing most of their TCP area over the ocean, and 2) TC centers over the ocean with their TCP area mostly over the land. In other words, under certain circumstances, Near-Land II and Overland I might not necessarily follow a strict chronological order because the TC center (as reported in the best track) does not coincide with the geometric center of each TCPF due to the complex coexisting factors that affect the shape of the precipitating area at landfall.

About Overland II and Overland III, there is a noticeable decrease in the average rainfall intensity as the storm moves into the land (Fig. 2 and axisymmetric profiles in Figs. 3 and 4). This behavior is consistent with the overall weakening observed in TCs during their final life cycle stages.

Regarding the radial distribution by basins, WNP shows the maximum rate of reduction in the Overland categories, though its final Overland intensity reaches a similar level to other global basins. An interesting feature in the global comparison is that ATL storms exhibit an apparent increase in the region near 300 km. However, further analysis reveals this feature could be the consequence of the combination of both scenarios: TCs with weak precipitation in the outer region disappeared at the Overland III stage, and relatively strong TCs with relatively intense rainfall near 300 km from the center survived at the Overland III stage. In addition, ATL profiles reveal a more drastic reduction in the rainfall rates across the inner-core area for the Overland II and Overland III stages.

d. TC Volumetric rain for over land stages

Considering after-landfall (Overland) stages are the most influential to human activities, a more detailed look at rainfall production is presented for such a portion of the TCP life cycle. Figure 5 shows the variation of the TC average rainfall rates, rain area, and volumetric rain as a function of intensity. Figures 5a and 5b describe the variation for the full extent of the average TCPF over both land and ocean. It can be noticed that in all the cases, the mean rate, mean rain area, and volumetric rain decrease systematically with the weakening of the TC intensity after landfall. However, when the portion over the ocean is removed (as shown in the procedure of Fig. 6), the observed trend of the TCP area increases as the TC intensity weakens (Fig. 5c). In other words, stronger TCs tend to have higher precipitation within smaller TC rainfall areas (i.e., TC precipitation over land is characterized by cases with high rainfall rates over a limited area and cases with low rainfall rates over a wide area). A potential explanation for the increase in the rainfall area with weaker systems is that the area for CAT2-CAT5 centers must be close to the coast before experiencing the weakening of maximum winds, while TD-CAT1 centers could be much farther inland to have the same effect. With the former being much closer to the coast, only about half of the area would be over land versus weaker systems farther inland. Regarding the volumetric rain, Fig. 5d shows the global average as a function of the TC intensity. Interestingly, it can be noticed that despite the reduction in the rain rate, the net amount of volumetric rain remains almost constant throughout all the intensity categories, with a minor increasing trend, having its maximum values for CAT1 and TS events. However, this apparent peak has low statistical significance as shown by the dispersion on the boxplots in Fig. 5d.

Based on the above results, calculations of combinations of the point (current) intensity versus LMI were performed for the volumetric rain calculations over two different areas of influence: 1) total TCP area (Fig. 7), and 2) the portion of the TCP that lies over the land (Tables 5 and 6).

Concerning the volumetric rain over the entire TCP area, Fig. 7 shows that when combining the contributions between both sections (ocean and land), it is difficult to establish a well-defined pattern in the global averages and the interbasin differences. However, it can be noticed that volumetric rain in the point-intensity–LMI approach generally increases with the point-intensity category (first part of the index). In addition, this trend is subsequently modulated by variations of the LMI, in which the volumetric rain reaches maximum values

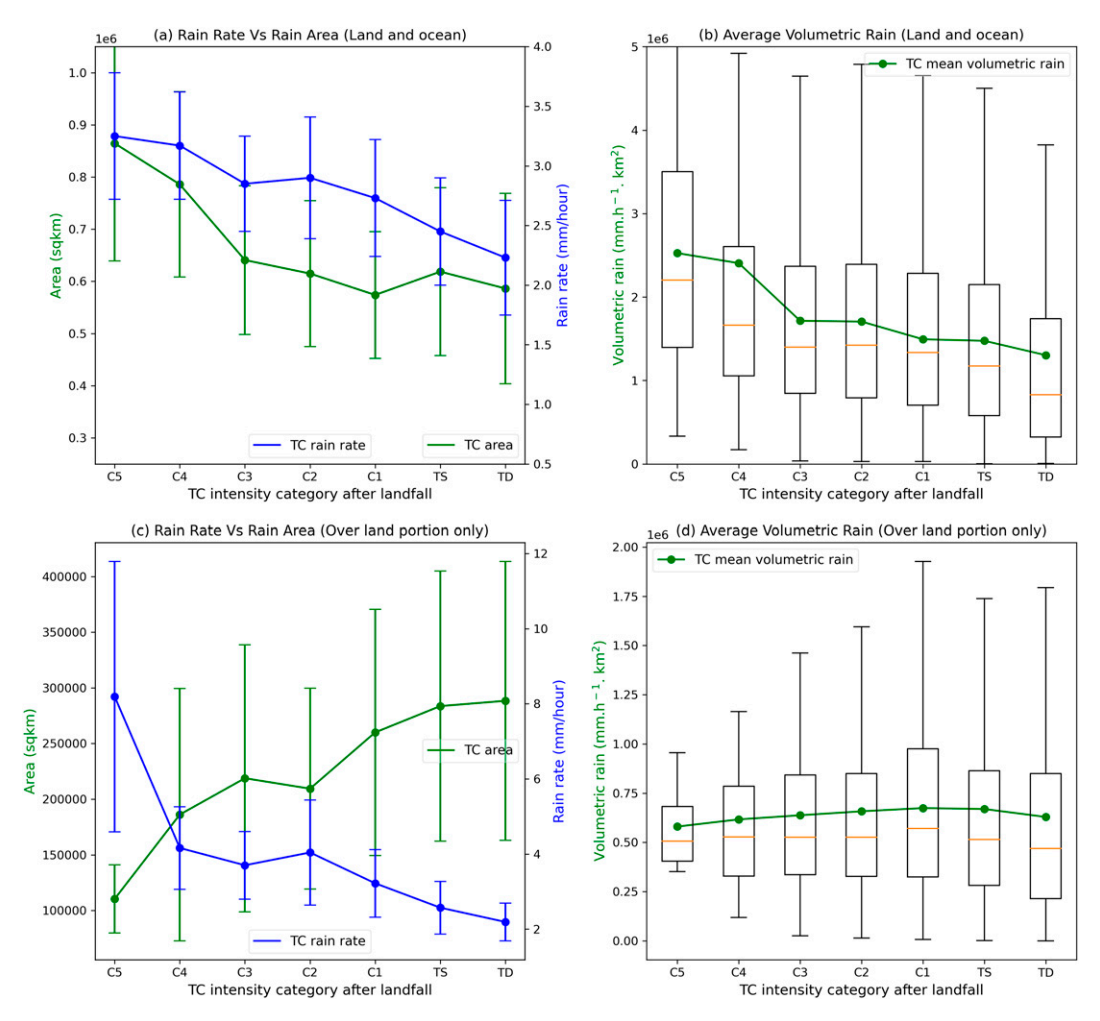


FIG. 5. Global variations of tropical cyclone rain rates, area, and volumetric rain for Overland stages: (a),(b) The variation considering the total TC extent in the calculations. (c),(d) The calculations by only considering the TC extent over the land portion. Vertical bars in left-hand side panels represent 1 standard deviation on each direction with reference to the average value. Boxplots and green lines in the right-hand side panels show statistics for volumetric rain calculations.

when the point intensity is equal to the LMI (e.g., TS/TS, CAT12/CAT12, and CAT35/CAT35). Interestingly, the minimum volumetric values are obtained for the combinations with pronounced gradients such as TD/CAT12, TS/CAT35, and CAT12/CAT35.

When the same analysis is performed over the portion of land only, global averages show that at least in ATL, ECPA, WNP, and SPA storms with an LMI of a major hurricane that makes landfall as either a TS or a TD they usually produce the most volumetric rain (Table 5, see bold numbers). At first look, this result seems opposite to Jiang et al. (2008), which showed that the TC volumetric rain decreases with TC current intensity as the storm makes landfall (i.e., TS and TD produced less volumetric rain). However, Jiang et al.'s (2008) results were for both overland and over-ocean portions of the TC rain, similar to the procedure followed to obtain Fig. 5a. Therefore, a distinction between the total precipitation produced by a TC and its isolated part over the land is a must

to understand the connection and the differences between studies that use information over the land (like rain gauges used by Touma et al. 2019) and satellite observations (e.g., Jiang et al. 2008 and this study) covering both the land and the ocean portions.

With reference to relationship between rain-rate intensity, TCP area, volumetric rain at global scale (Table 6), our findings partially agree with the study of Touma et al. (2019), which suggested that the highest rainfall intensity and the largest rainfall area over land occur when major hurricanes have weakened and made landfall as tropical storms. Their finding is consistent with our results of the rainfall area in Table 6. However, in terms of the rainfall intensity component, we found that highest overland rainfall intensity is from the CAT35/CAT35 category. Not only the current TC intensity is important for overland rainfall intensity, but the LMI is also critical. Highest TC overland rainfall intensity, raining area, and volumetric rain are all from TCs with an LMI of

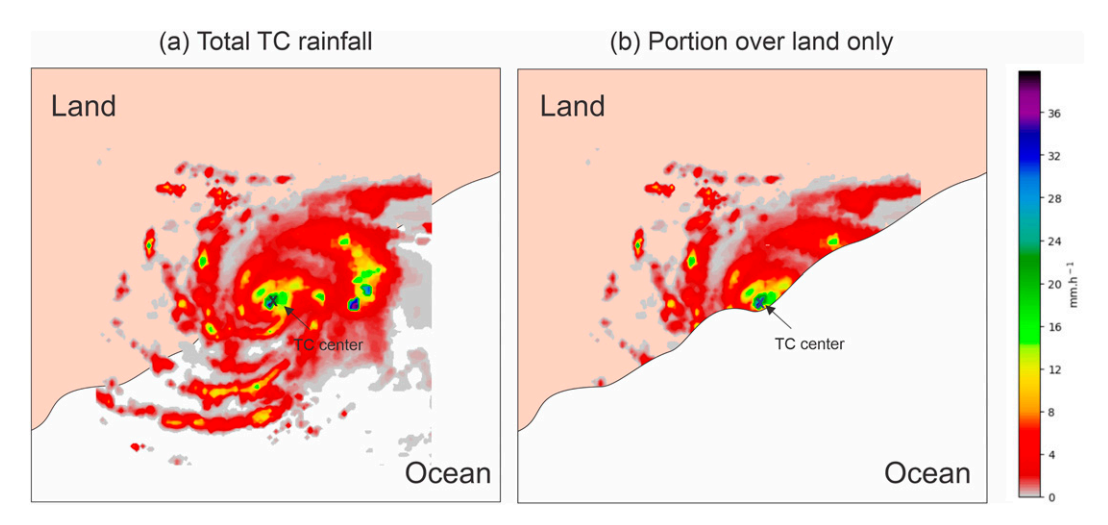


FIG. 6. Differentiation between tropical cyclone precipitation for Overland stages: (a) calculation over the total storm area and (b) calculation over the land portion only.

major hurricane strength. The averaged rain rate increases with LMI when the current intensity is the same.

Touma et al. (2019) derived the TC rainfall data from the meteorological rain gauge stations measuring the daily accumulated precipitation (an increase in the volume of water in the rain gauge in millimeters). Their "rainfall intensity" was actually defined as "daily accumulation mm day⁻¹," not the real instantaneous rainfall intensity as measured by satellite. Here we have opposite results in the scenario in which we compare Touma's TC rain intensity with the rain rates reported in Table 6. It can be noticed that the rain-rate intensity over the land is still highly dependent on the TC wind intensity, as demonstrated in the results of Fig. 5c and the average rain-rate column presented in Table 6. Another possible

reason for the inconsistency between this study and Touma et al. (2019) study is that rain gauge data might underestimate rainfall from major hurricanes because rain gauges could be destroyed by the strong winds.

Another important difference to consider between both studies is the temporal resolution of the data. Touma et al. (2019) used the TC rainfall data from meteorological rain gauges that reported daily accumulations that match TC tracks at 1200 UTC. In contrast, this study uses satellite observations with the intensity obtained as the nearly instantaneous retrieval at the observation time (in mm h⁻¹) over the pixels contained in each TCPF every three hours. Therefore, with much higher temporal resolution and more robust sample sizes from the IMERG satellite, we conclude that the combination

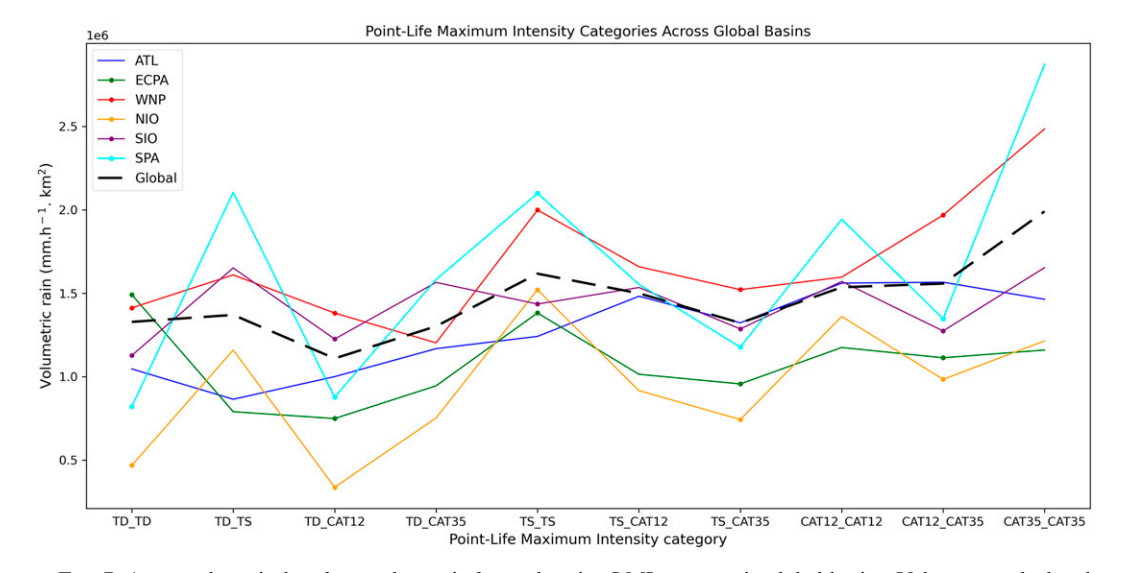


FIG. 7. Averaged tropical cyclone volumetric for each point–LMI category in global basins. Values are calculated over the entire TC area (including over ocean and over land) when the storm best-track center was over land (Overland stages).

TABLE 5. Averaged tropical cyclone volumetric rain [thousands, i.e. (mm km² h⁻¹)/1000] and number of overpasses samples (in parentheses) for each point–LMI category in global basins. Values are calculated over the portion of TC rain over land only.

Point intensity/LMI	ATL	ECPA	WNP	NIO	SIO	SPA	Global
TD/TD	491 (27)	513 (15)	516 (66)	241 (22)	773 (15)	233 (21)	596 (146)
TD/TS	495 (326)	333 (37)	686 (268)	567 (135)	706 (217)	613 (122)	599 (1105)
TD/CAT12	573 (80)	269 (25)	674 (122)	249 (36)	489 (126)	378 (10)	524 (399)
TD/CAT35	770 (101)	789 (25)	742 (82)	523 (21)	619 (117)	931 (41)	730 (387)
TS/TS	464 (154)	463 (43)	722 (181)	797 (68)	550 (105)	518 (51)	621 (602)
TS/CAT12	596 (166)	410 (24)	702 (248)	669 (52)	615 (126)	363 (16)	635 (632)
TS/CAT35	881 (132)	618 (33)	777 (250)	650 (45)	584 (148)	762 (45)	718 (653)
CAT12/CAT12	752 (22)	440 (14)	590 (65)	779 (9)	811 (15)	418 (4)	652 (129)
CAT12/CAT35	632 (76)	554 (21)	647 (156)	741 (31)	755 (104)	575 (38)	603 (426)
CAT35/CAT35	441 (28)	523 (4)	636 (58)	760 (10)	728 (24)	742 (6)	629 (130)

of decreasing precipitation intensity and increasing precipitating area as the TC intensity decreases when making landfall explains the maxima of point-LMI events with TD/CAT35 or TS/CAT35.

An alternative and potential explanation for the TD/CAT35 and TS/CAT35 maxima can be found in the average rain rates and the average percentage of rain area over land in Table 6. From the rain-rate perspective, it can be noticed that point-intensity–LMI categories still are highly dependent on both the current TC intensity and LMI (i.e., TD/TD with the minimum values and CAT35/CAT35 with the maximum). However, once the percentage over land is analyzed, it is evident that the most intense categories reached less rainy areas over the land due to its rain concentration around the TC center, in contrast with TDs and TS with more sparse precipitation (bigger TC rain areas). The combination of these two factors leads to a rain balance that results in maximum values for TDs/TSs with the largest raining areas with a history of high precipitation intensity, as produced by major hurricanes.

e. Environmental effects during landfalling stages

Variations of rainfall magnitude for each landfalling stage are analyzed for different TC translation speeds and environmental conditions. Figure 8 shows a set of 2D shear-relative TC rainfall composites describing the average influence of each variable differentiating between high/low values at different

landfall stages. In terms of rainfall magnitude, previous investigations suggested that higher values in the storm motion speed (Burpee and Black 1989; Lonfat et al. 2004), sea surface temperature (Lin et al. 2015), total precipitable water (Jiang et al. 2008; Hill and Lackmann 2009), and low vertical wind shear (Cecil 2007; Corbosiero and Molinari 2002; Wingo and Cecil 2010) boost the precipitation production. Our results shown in Fig. 8, for each of the above variables, confirm that these conclusions remain valid for all the landfalling stages (that accounts for the TCP area and distance from the coast) suggested in this paper.

In terms of the location of the most prominent rainfall rates, Fig. 8 shows that in landfalling TCs, the maximum values are concentrated downshear to downshear-left relative to the vertical wind shear direction. This result is consistent with previous researchers that found the same pattern for TC precipitation over the ocean (Chen et al. 2006; Cecil 2007; Jiang et al. 2008; Xu et al. 2014; Pei and Jiang 2018) and over the land in localized regions (i.e., Xu et al. 2014 over China). In this study, we ratify that a downshear to downshear-left pattern remains valid for the Open Ocean, Adjacent to the Coast, and Overland landfall stages on a global scale.

In general, it can be observed that the maximum intensity values occur in the Adjacent to the Coast categories when exposed to high TC speed, TPW, and SST. Likewise, the minimum intensity values occur across the Overland categories when

TABLE 6. Averaged tropical cyclone volumetric rain and samples size for each point-LMI category in global basins. Values are calculated over the portion of TC rain over land (Overland I, Overland II, and Overland III). Standard deviation is expressed as percentage of the average.

Point intensity/LMI	Sample size	Avg rain rate (mm h ⁻¹)	Avg TC area (km ²)	Volumetric rain (mm km ² h ⁻¹)	Avg percentage of rain area over land
TD/TD	146	$2.13\% \pm 10\%$	$267508\pm25\%$	595 715 ± 31%	61%
TD/TS	1105	$2.18\% \pm 8\%$	$283009\pm22\%$	$599036\pm24\%$	64%
TD/CAT12	399	$2.22\% \pm 9\%$	$251954\pm17\%$	$524224 \pm 27\%$	62%
TD/CAT35	387	$2.37\% \pm 13\%$	$349138\pm15\%$	$729524 \pm 19\%$	67%
TS/TS	602	$2.50\% \pm 14\%$	$274831\pm29\%$	$621434\pm32\%$	51%
TS/CAT12	632	$2.60\% \pm 14\%$	$273169\pm23\%$	$634463 \pm 31\%$	52%
TS/CAT35	653	$2.62\% \pm 16\%$	$301909\pm22\%$	$718013 \pm 32\%$	58%
CAT12/CAT12	129	$3.37\% \pm 15\%$	$254426 \pm 21\%$	$651937\pm25\%$	41%
CAT12/CAT35	426	$3.46\% \pm 14\%$	$243429 \pm 20\%$	$702966\pm22\%$	43%
CAT35/CAT35	130	$3.97\% \pm 10\%$	$205698 \pm 15\%$	$629466\pm21\%$	31%

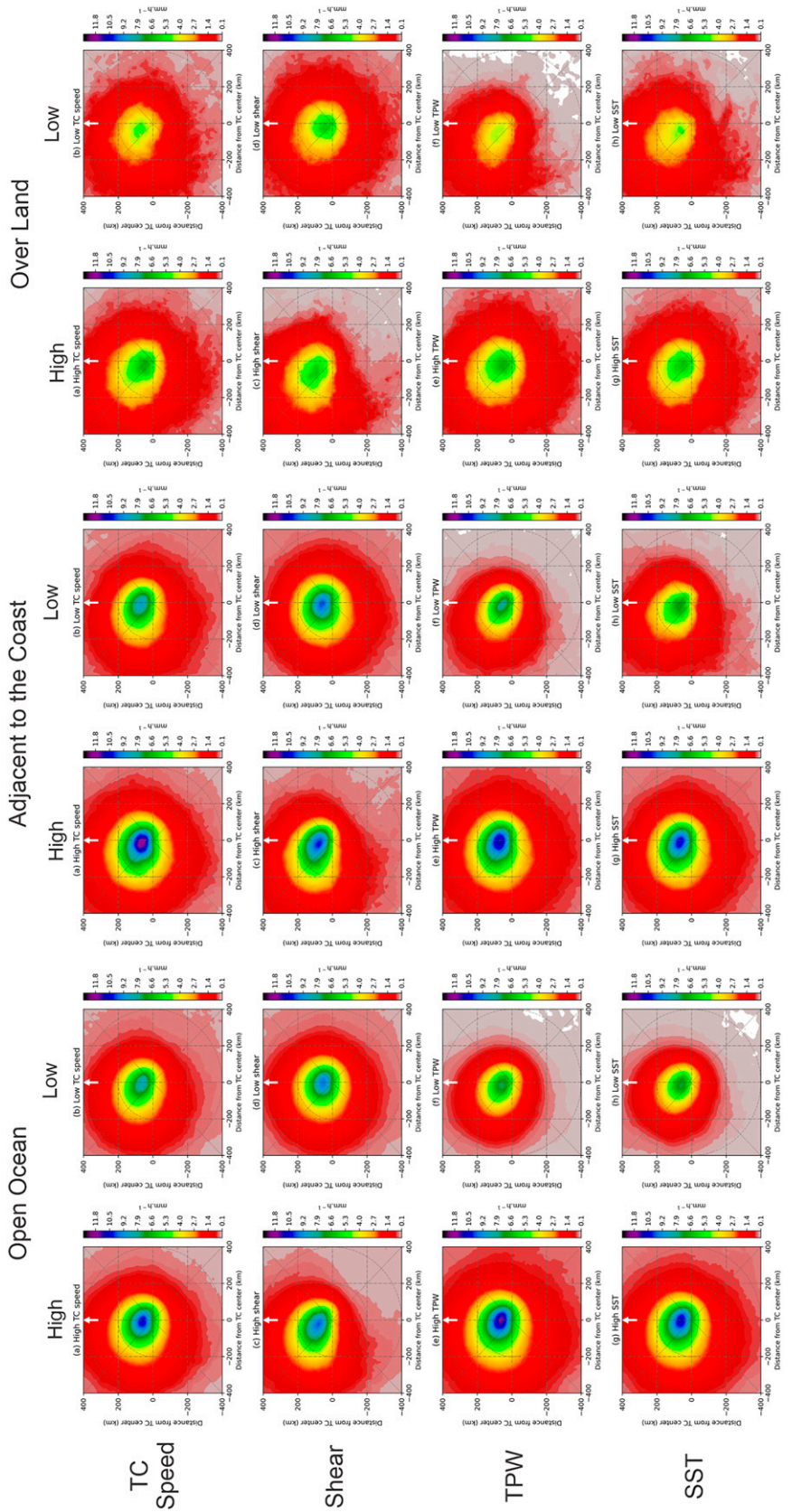


FIG. 8. 2D composites of shear-relative rainfall rate produced by TCs in the different landfalling stages for low/high storm motion speeds, low/high-shear magnitudes, low/high TPWs, and low/high SSTs. In all panels, the direction of environmental vertical wind shear points upward as indicated by the white arrow.

exposed to low values of the same variables. However, it is also noticed that the reduction of the intensity at Overland stages is accompanied by a general spread of the TCP from the areas of high concentration in the Adjacent to the Coast and Open Ocean stages, that is, plots showing Overland rainfall exhibit more disorganized patterns but preserving clusters of rain near their original position before landfall. This result is consistent with the findings of Yu et al. (2015), in which the author indicates that the axisymmetric component (observed in the wavenumber 0) is preserved but rapidly decreases after landfall.

As for the TC rainfall asymmetries, we can see from Fig. 8 that the mean rainfall pattern of TCs under high shear is more asymmetric than that of TCs under low shear for TCs for over ocean, near-coast, and after-landfall stages. This indicates that shear is the dominant factor for rainfall asymmetries even for after-landfall stages. Previous studies have shown that land surface can cause TC rainfall structure to be asymmetric (e.g., Chan and Liang 2003; Chen and Yau 2003; Chan et al. 2004; Kimball 2008). This is consistent with Fig. 8, which shows that the rainfall pattern is more asymmetric under high-shear conditions for the Overland stage than that for over Open Ocean and Near-Land stages.

4. Conclusions

The climatological averages of TCP rainfall over the open ocean, adjacent to the coast, and over the land on a global basis are investigated using rainfall estimations from IMERG TRMM/GPM satellite data during 2000–19. A new approach that combines the TCP area and the distance from the coast is proposed to characterize the TC rain magnitude at different landfall stages. Our observational results show that across the Ocean, Offshore, and Near-Land categories, TCP experiences a homogeneous enhancement controlled by the portion of the TC that remains over the ocean. Once the TCP area has reached at least 50% over the land, the overall precipitations rates begin to decay and the precipitation areas over land begin to expand, following a nearly perfect inversely proportional relation. This pattern is constant for all the landfalling stages until the TC totally disappears.

An important finding is that the TC rainfall intensity peaks at the Near-Land I stage with a secondary peak in the average rainfall rate at the Overland I landfalling stage. However, data with higher temporal resolution is required for a more detailed precipitation analysis in the two proposed categories around the exact landfall event (Near-Land II and Overland I). Adopting an additional time-based criterion could help to refine the analysis and explain the mechanisms behind this finding. Besides, an error assessment of the satellite precipitation retrievals in the transition area between the land and the ocean for extreme precipitation events (like TCs) is a must to verify the accuracy and order of magnitude of this finding. Unfortunately, due to the diverse nature of measurement sources and retrieval algorithms, characterizing errors associated with the IMERG product is not a simple task. So, this might be a good direction for new research.

In the case of the Overland stages, our findings demonstrate that when the combined contribution of the TC rainfall over the land and the ocean is analyzed (Fig. 6a), there are regular decreases in the rainfall rate and the volumetric rain as the storm area moves inland, consistent with Jiang et al. (2008). However, once the rainfall over the land is analyzed independently (Fig. 6b), the volumetric rainfall slightly increases as the storm's intensity decreases while making landfall, finding maxima for CAT1 and TS. Further observational analysis using the concept of point-LMI categories demonstrates that TCs that at some point in their life cycle reached major hurricane strength and make landfall as TS or TD produced the highest volumetric rain over the land surface. This finding refines the previous investigation by Touma et al. (2019) that suggested that this effect was due to intensity and areal variations, but clarifying that the rainfall intensity over land still decreases as the storm's intensity decreases during landfall while the volumetric rain increases due to the increase of raining area over land. We also found that the lifetime maximum intensity (LMI) of a TC is critical to determine its flooding potential over land.

For the influence of environmental conditions, this research reaffirms that higher SST, TPM, and translation speed, combined with low VWS boost the precipitation production regardless of the landfalling stage. In addition, the precipitation maximum is located downshear to downshear left of the TC center regardless of the distance from the shore or the percentage of TCP area over the land, over all global basins. These findings are consistent with investigations focused on TCs over the ocean and some basin-localized landfall studies. Results of this study are useful for a better understanding of TCP at different landfall stages.

Acknowledgments. The authors thank Dr. Chris Landsea and another anonymous reviewer for their helpful comments, which led to substantial improvement of the paper. This work was supported by the Fulbright-Colciencias grant as part of the cultural exchange program between the United States of America and the Republic of Colombia. This research was also partially supported by NSF Grant 1947304 under the direction of Drs. Jielun Sun and Yu Gu and NASA Weather and Atmospheric Dynamics (WAAD) Grant NNX17AH72G under the direction of Drs. Ramesh Kakar, Gail Jackson, Tsengdar Lee, and Will McCarty.

Data availability statement. This paper uses three main sources of information: 1) Satellite data openly available through the NASA Precipitation Processing System servers (IMERG product; ftp://arthurhou.pps.eosdis.nasa.gov/gpmdata/YYYY/MM/DD/imerg/), 2) GIS and tabular data from the open repository of the IBTrACS project archive available at the website of the NOAA National Centers for Environmental Information, and 3) The SHIPS developmental database from Colorado State University for all global TC-prone basins (5-day predictors; https://rammb.cira.colostate.edu/research/tropical_cyclones/ships/developmental_data.asp). DOIs and further details on the data sources have been properly cited and provided in the main article and the references section.

REFERENCES

- Bagtasa, G., 2017: Contribution of tropical cyclones to rainfall in the Philippines. J. Climate, 30, 3621–3633, https://doi.org/10.1175/ JCLI-D-16-0150.1.
- Bregy, J. C., J. T. Maxwell, S. M. Robeson, J. T. Ortegren, P. T. Soulé, and P. A. Knapp, 2020: Spatiotemporal variability of tropical cyclone precipitation using a high-resolution, gridded (0.25° × 0.25°) dataset for the eastern United States, 1948–2015. J. Climate, 33, 1803–1819, https://doi.org/10.1175/JCLI-D-18-0885.1.
- Burpee, R. W., and M. L. Black, 1989: Temporal and spatial variations of rainfall near the centers of two tropical cyclones. *Mon. Wea. Rev.*, **117**, 2204–2218, https://doi.org/10.1175/1520-0493(1989)117<2204:TASVOR>2.0.CO;2.
- Cecil, D. J., 2007: Satellite-derived rain rates in vertically sheared tropical cyclones. *Geophys. Res. Lett.*, 34, L02811, https://doi. org/10.1029/2006GL027942.
- Chan, J. C. L., and X. Liang, 2003: Convective asymmetries associated with tropical cyclone landfall. Part I: f-plane simulations. *J. Atmos. Sci.*, 60, 1560–1576, https://doi.org/10.1175/1520-0469(2003)60<1560:CAAWTC>2.0.CO;2.
- —, K. S. Liu, S. E. Ching, and E. S. T. Lai, 2004: Asymmetric distribution of convection associated with tropical cyclones making landfall along the South China coast. *Mon. Wea. Rev.*, 132, 2410–2420, https://doi.org/10.1175/1520-0493(2004)132<2410: ADOCAW>2.0.CO;2.
- Chen, S. S., J. A. Knaff, and F. D. Marks Jr., 2006: Effects of vertical wind shear and storm motion on tropical cyclone rainfall asymmetries deduced from TRMM. *Mon. Wea. Rev.*, 134, 3190–3208, https://doi.org/10.1175/MWR3245.1.
- Chen, Y., and M. K. Yau, 2003: Asymmetric structures in a simulated landfalling hurricane. *J. Atmos. Sci.*, **60**, 2294–2312, https://doi.org/10.1175/1520-0469(2003)060<2294:ASIASL>2. 0.CO;2.
- Corbosiero, K. L., and J. Molinari, 2002: The effects of vertical wind shear on the distribution of convection in tropical cyclones. *Mon. Wea. Rev.*, 130, 2110–2123, https://doi.org/10.1175/ 1520-0493(2002)130%3C2110:TEOVWS%3E2.0.CO;2.
- Dare, R., N. Davidson, and J. Mcbride, 2012: Tropical cyclone contribution to rainfall over Australia. *Mon. Wea. Rev.*, 140, 3606–3619, https://doi.org/10.1175/MWR-D-11-00340.1.
- DeMaria, M., and J. Kaplan, 1994: A Statistical Hurricane Intensity Prediction Scheme (SHIPS) for the Atlantic Basin. *Wea. Forecasting*, **9**, 209–220, https://doi.org/10.1175/1520-0434(1994)009<0209:ASHIPS>2.0.CO;2.
- —, and —, 1999: An updated Statistical Hurricane Intensity Prediction Scheme (SHIPS) for the Atlantic and eastern North Pacific basins. Wea. Forecasting, 14, 326–337, https://doi.org/10. 1175/1520-0434(1999)014<0326:AUSHIP>2.0.CO;2.
- —, M. Mainelli, L. K. Shay, J. A. Knaff, and J. Kaplan, 2005: Further improvements to the Statistical Hurricane Intensity Prediction Scheme (SHIPS). Wea. Forecasting, 20, 531–543, https://doi.org/10.1175/WAF862.1.
- Hill, K. A., and G. M. Lackmann, 2009: Influence of environmental humidity on tropical cyclone size. *Mon. Wea. Rev.*, 137, 3294–3315, https://doi.org/10.1175/2009MWR2679.1.
- Holland, G. J., 1980: An analytic model of the wind and pressure profiles in hurricanes. *Mon. Wea. Rev.*, 108, 1212–1218, https://doi.org/10.1175/1520-0493(1980)108<1212:AAMOTW>2.0.CO;2.
- —, J. I. Belanger, and A. Fritz, 2010: A revised model for radial profiles of hurricane winds. *Mon. Wea. Rev.*, **138**, 4393–4401, https://doi.org/10.1175/2010MWR3317.1.

- Huffman, G. J., E. F. Stocker, D. T. Bolvin, E. J. Nelkin, J. Tan, 2019: GPM IMERG final precipitation L3 half hourly 0.1-degree × 0.1-degree V06. Goddard Earth Sciences Data and Information Services Center (GES DISC), accessed 3 June 2021, https://doi.org/10.5067/GPM/IMERG/3B-HH/06.
- —, and Coauthors, 2020: Integrated Multi-satellitE Retrievals for the Global Precipitation Measurement (GPM) Mission (IMERG). Satellite Precipitation Measurement, Advances in Global Change Research, Vol. 67, Springer, 343–353, https:// doi.org/10.1007/978-3-030-24568-9_19.
- Jiang, H., and E. J. Zipser, 2010: Contribution of tropical cyclones to the global precipitation from eight seasons of TRMM data: Regional, seasonal, and interannual variations. *J. Cli*mate, 23, 1526–1543, https://doi.org/10.1175/2009JCLI3303.1.
- —, J. B. Halverson, and E. J. Zipser, 2008: The influence of environmental moisture on TRMM-derived tropical cyclone precipitation over land and ocean. *Geophys. Res. Lett.*, 35, L17806, https://doi.org/10.1029/2008GL034658.
- Kaplan, J., and M. DeMaria, 1995: A simple empirical model for predicting the decay of tropical cyclone winds after landfall. *J. Appl. Meteor.*, 34, 2499–2512, https://doi.org/10.1175/1520-0450(1995)034<2499:ASEMFP>2.0.CO;2.
- Kimball, S. K., 2008: Structure and evolution of rainfall in numerically simulated landfalling hurricanes. *Mon. Wea. Rev.*, 136, 3822–3847, https://doi.org/10.1175/2008MWR2304.1.
- Knapp, K. R., H. J. Diamond, J. P. Kossin, M. C. Kruk, C. J. Schreck, 2018: International Best Track Archive for Climate Stewardship (IBTrACS) Project, version 4 [subset from 1998 to 2016]. NOAA National Centers for Environmental Information, accessed 30 May 2021, https://doi.org/10.25921/82ty-9e16.
- Lin, Y., M. Zhao, and M. Zhang, 2015: Tropical cyclone rainfall area controlled by relative sea surface temperature. *Nat. Commun.*, 6, 6591, https://doi.org/10.1038/ncomms7591.
- Lonfat, M., F. D. Marks Jr., and S. S. Chen, 2004: Precipitation distribution in tropical cyclones using the Tropical Rainfall Measuring Mission (TRMM) microwave imager: A global perspective. *Mon. Wea. Rev.*, 132, 1645–1660, https://doi.org/ 10.1175/1520-0493(2004)132%3C1645:PDITCU%3E2.0.CO;2.
- Matyas, C. J., 2010: Associations between the size of hurricane rain fields at landfall and their surrounding environments. *Meteor. Atmos. Phys.*, **106**, 135–148, https://doi.org/10.1007/s00703-009-0056-1.
- Pei, Y., and H. Jiang, 2018: Quantification of precipitation asymmetries of tropical cyclones using 16-year TRMM observations. J. Geophys. Res. Atmos., 123, 8091–8114, https://doi.org/10.1029/2018JD028545.
- Prat, O. P., and B. R. Nelson, 2016: On the link between tropical cyclones and daily rainfall extremes derived from global satellite observations. *J. Climate*, 29, 6127–6135, https://doi.org/10.1175/JCLI-D-16-0289.1.
- Rappaport, E. N., 2000: Loss of life in the United States associated with recent Atlantic tropical cyclones. *Bull. Amer. Meteor. Soc.*, **81**, 2065–2074, https://doi.org/10.1175/1520-0477(2000)081<2065:LOLITU>2.3.CO;2.
- Ren, F., G. Wu, W. Dong, X. Wang, Y. Wang, W. Ai, and W. Li, 2006: Changes in tropical cyclone precipitation over China. *Geophys. Res. Lett.*, 33, L20702, https://doi.org/10.1029/2006GL027951.
- Rodgers, E. B., S. W. Chang, and H. F. Pierce, 1994: A satellite observational and numerical study of precipitation characteristics in western North Atlantic tropical cyclones. *J. Appl. Meteor.*, 33, 129–139, https://doi.org/10.1175/1520-0450(1994)033<0129: ASOANS>2.0.CO;2.

- Schumacher, A., M. DeMaria, and J. Knaff, 2013: Summary of the new statistical-dynamical intensity forecast models for the Indian Ocean and Southern Hemisphere and resulting performance. JTWC Project Final Rep., 1–11, https://rammb.cira.colostate.edu/research/tropical_cyclones/ships/docs/JTWC_project final report oct 2013.docx.
- Touma, D., S. Stevenson, S. J. Camargo, D. E. Horton, and N. S. Diffenbaugh, 2019: Variations in the intensity and spatial extent of tropical cyclone precipitation. *Geophys. Res. Lett.*, 46, 13992–14002, https://doi.org/10.1029/2019GL083452.
- Uddin, M., Y. Li, K. K. Cheung, Z. M. Nasrin, H. Wang, L. Wang, and Z. Gao, 2019: Rainfall contribution of tropical cyclones in the Bay of Bengal between 1998 and 2016 using TRMM satellite data. *Atmosphere*, 10, 699, https://doi.org/10.3390/atmos10110699.
- Willoughby, H. E., 2012: Distributions and trends of death and destruction from hurricanes in the United States, 1900–2008. *Nat. Hazards Rev.*, 13, 57–64, https://doi.org/10.1061/(ASCE)NH. 1527-6996.0000046.

- Wingo, M. T., and D. J. Cecil, 2010: Effects of vertical wind shear on tropical cyclone precipitation. *Mon. Wea. Rev.*, 138, 645– 662, https://doi.org/10.1175/2009MWR2921.1.
- Xu, W., H. Jiang, and X. Kang, 2014: Rainfall asymmetries of tropical cyclones prior to, during, and after making landfall in South China and southeast United States. Atmos. Res., 139, 18–26, https://doi.org/10.1016/j.atmosres. 2013.12.015.
- Yu, Z., Y. Wang, and H. Xu, 2015: Observed rainfall asymmetry in tropical cyclones making landfall over China. J. Appl. Meteor. Climatol., 54, 117–136, https://doi.org/10.1175/JAMC-D-13-0359.1.
- —, —, N. Davidson, Y. Chen, Y. Chen, and H. Yu, 2017: On the relationship between intensity and rainfall distribution in tropical cyclones making landfall over China. J. Appl. Meteor. Climatol., 56, 2883–2901, https://doi.org/10.1175/JAMC-D-16-0334.1.
- Zhang, Q., X. Gu, P. Shi, and V. P. Singh, 2017: Impact of tropical cyclones on flood risk in southeastern China: Spatial patterns, causes and implications. *Global Planet. Change*, **150**, 81–93, https://doi.org/10.1016/j.gloplacha.2017.02.004.